Renewable Energy 179 (2021) 1618–1635

Contents lists available at ScienceDirect

Renewable Energy

journal homepage: www.elsevier.com/locate/renene

A comparative study of fully coupled and de-coupled methods on dynamic behaviour of floating wind turbine drivetrains

Shuaishuai Wang [a, *], Torgeir Moan [a, b], Amir R. Nejad [a]

[a] Department of Marine Technology, Norwegian University of Science and Technology (NTNU), Norway
[b] Centre for Autonomous Marine Operations and Systems (AMOS), Department of Marine Technology, NTNU, Trondheim NO, 7491, Norway

ARTICLE INFO

Article history:
Received 15 January 2021
Received in revised form
28 July 2021
Accepted 29 July 2021
Available online 3 August 2021

Keywords:
Floating wind turbine
Drivetrain
Fully coupled method
De-coupled method
Fatigue damage
Comparative study

ABSTRACT

Traditionally, drivetrain responses are obtained by a de-coupled analysis, which first involves a global analysis with a simplified representation of the drivetrain, followed by a detailed analysis of the drivetrain with the input of global response on the drivetrain interface. As the wind turbine size increases, it is questionable whether this de-coupled analysis method yields sufficiently accurate results. To address this question, a comparative study of the drivetrain dynamic behaviour obtained by a fully coupled method and a de-coupled one, is conducted and reported in this paper. A 10-MW fully coupled aero-hydro-servo-elastic floating wind turbine dynamic model is developed, including a high-fidelity drivetrain. The developed fully coupled model is assessed to be reasonable via the comparison of drivetrain first-order natural frequency and code-to-code comparisons in terms of global responses between two simulation tools Simpack and Fast. Resonance analysis of the 10-MW drivetrain in the fully coupled model is performed, with focus on rotor-drivetrain-bedplate-tower coupled modes in the low frequency range. Time domain simulations of the drivetrain in the fully coupled and the de-coupled models are carried out in different environmental conditions. One-hour fatigue damage of drivetrain gears and bearings in the fully coupled and de-coupled models are compared. Effect of nacelle motion on drivetrain fatigue damage in the de-coupled analysis is discussed. The results are presented to demonstrate whether the de-coupled method could be confidently used for drivetrain dynamic analysis. This study provides a basis for drivetrain design and dynamic analysis in floating wind turbines.

1. Introduction

In recent years, floating offshore wind turbines have rapidly been developing to harvest the vast offshore wind resources in deep water. However, the cost of wind energy in deep water sites still need to be reduced. As one of the economically feasible solutions, increasing wind turbine rating has attracted great interests from both the commercial markets and the research communities. A number of large-scale floating wind turbine (FWT) concepts have emerged, e.g. MHI Vestas V174 9.5-MW and V164 10.0-MW [1], LIFES50+ OO-Star Wind Floater Semi 10-MW [2], GE's Haliade-X 12-MW [3] and IEA Wind 15-MW [4]. Simultaneously significant progress has been made in design, optimization and numerical analysis of blade, tower, support structure and mooring system, as demonstrated in studies [5–7].

However, much less information about drivetrains in FWTs is publicly available. During the past decade, high-speed geared and direct-driven drivetrains are dominating in the market, while both have their pros and cons in terms of material costs, weight, reliability and maintenance costs and which one is the best choice is not yet achieved. The limitations of the traditional high-speed and direct-driven drivetrains facilitate the development of a novel drivetrain concept, namely medium-speed drivetrain, which could effectively balance the reliability and material cost and it is therefore believed to be a very promising alternative in offshore applications. Up to now, some attempts to use the medium-speed drivetrain concept have emerged in the industry and academic communities, e.g. Vestas EnVentus V162–5.6 MW [8], MHI Vestas V174 9.5-MW and V164–10.0 MW [1] as well as DTU 10-MW [9]. This implies that geared drivetrains will continue to be widely used in the future. However, an essential challenge in the geared drivetrains that needs to be addressed is the high failure risks and downtime caused by drivetrain mechanical components. It has been reported that failures of the gearbox would lead to significant

* Corresponding author.
E-mail address: shuaishuai.wang@ntnu.no (S. Wang).

https://doi.org/10.1016/j.renene.2021.07.136

downtime based on a survey of over 64000 maintenance and repair reports from 1500 onshore wind turbines [10]. Although there is still insufficient data to demonstrate the reliability of drivetrains in FWTs, it is reasonable to expect a high failure rate due to the additional wave effect and immature technology. Moreover, because of the limited accessibility, larger maintenance and repair costs of FWT drivetrains are expected than those of the land-based turbines. Therefore, it is of great significance to get deeper insight into the drivetrain dynamic behaviour, thus to improve its reliability and reduce the costs.

Some studies on dynamic analysis of drivetrains in FWTs have been conducted. Xing et al. [11] studied the dynamics of the National Renewable Energy Laboratory (NREL) 750-kW drivetrain in a spar-type floating support system. Fatigue damage of a 5-MW drivetrain in land-based as well as TLP, spar and semi-submersible FWTs was compared in the study of Nejad et al. [12]. A 1.5 MW wind turbine drivetrain dynamic model was established by Li et al. [13] and its dynamic characteristics under pitch, surge and heave floating platform motions were studied. A high-fidelity medium-speed drivetrain for the Danmarks Tekniske Universitet (DTU)'s 10-MW wind turbine was designed and modelled by Wang et al. [14]. In addition, in their other works [15,16], effect of bedplate flexibility on the dynamic behaviour of the 10-MW drivetrain in a spar-type FWT was investigated; dynamic behaviour of the 10-MW drivetrain in bottom-fixed monopile and the spar-type floating wind turbines were compared. However, due to the limitations of simulation tools in modelling the drivetrain in sufficient detail and the potential excessive computational costs, most of studies on drivetrain dynamics up to now have been conducted based on a de-coupled method. This means that a global wind turbine analysis is first performed, based on a simple torsional degree-of-freedom (DOF) model for the drivetrain, followed by a local detailed drivetrain dynamic simulation, where loads and motions at boundary interface positions are provided by the global analysis. The de-coupled approach does not consider the feedback effect of detailed drivetrain model on global analysis. In traditional wind turbine drivetrain design, this approach was believed to be acceptable, because the drivetrain first-order torsional eigenfrequency is usually designed to be outside the range of rotor excitation frequencies and eigenfrequencies in the gearbox are much higher than the external excitation frequencies, making the drivetrain avoids resonance.

However, the acceptability of this simplification needs to be justified because of the following reasons. The drivetrain resonance in non-torsional directions are not checked in the de-coupled analysis. As presented in Table 5 in this paper, the first- and second-order drivetrain non-torsional natural frequencies are in the same order of magnitude as the first torsional natural frequency that is traditionally modelled, but their values are slightly lower than the first-order torsional natural frequency, which makes the drivetrain natural frequencies more close to the excitation frequency margin. Besides, as the size of wind turbine sub-systems and sub-components increases, the structural flexibility and mass properties are also increasing, which will make the coupled rotor-drivetrain-bedplate-tower eigenfrequencies lower, and thus drivetrain resonance risks in the non-torsional modes become higher. Therefore, it is essential to check the drivetrain non-torsional natural frequencies before the use of the de-coupled method, especially for large offshore wind turbines with large structural flexibility and mass properties. If drivetrain resonance happens in the fully coupled model, the de-coupled analysis method should not be used. Moreover, in addition to the external excitation from rotor side, the dynamic responses of the gearbox is also largely affected by the internal excitation due to the time-varying gear teeth stiffness and gear pair transmission errors. Whether the gearbox dynamics make negligible effects on global analysis remains to be revealed. In addition, the de-coupled wind turbine model considers the bedplate as a rigid body, whether the deformation of the flexible bedplate in the fully coupled wind turbine model make a certain effect on global analysis is also to be uncovered. According to the peer-reviewed literature on the wind turbine drivetrain study, only one study compared the drivetrain dynamic response between de-coupled and fully coupled models; Schkoda et al. [17] established a drivetrain dynamic model of a 1.6 MW land-based wind turbine and studied the influence of the abstraction of nacelle from the global model on dynamic response of the drivetrain. But the comparison based on the small land-based turbine is insufficient to represent the situation in large turbines. There is an increasing need to make a more comprehensive comparison for drivetrains in large-scale floating offshore wind turbines.

In light of the uncertainty implied by the de-coupled approach to the drivetrain dynamic analysis, a fully coupled method is compared with the de-coupled method in this study, to reveal whether the de-coupled method is still accurate enough for determining the load effects in drivetrains in large-scale offshore wind turbines. In fulfilment of this objective, a fully coupled aero-hydro-servo-elastic 10-MW FWT model that integrates with a high-fidelity drivetrain is established. The integrated fully coupled wind turbine model is validated via the comparisons of the drivetrain first-order torsional eigenfrequencies between numerical and theoretical calculations and code-to-code comparisons. Resonance analysis of the drivetrain in the fully coupled model is conducted, with focus on non-torsional modes. Fatigue damage of the drivetrain in the fully coupled and the de-coupled models are compared in different environmental conditions. Effect of nacelle motions on drivetrain fatigue damage is investigated in the de-coupled analysis. This study is a step forward of public research into design, modelling and analysis for wind turbine drivetrains.

2. Floating wind turbine and drivetrain concepts

2.1. 10-MW floating wind turbine concept

The DTU 10-MW reference wind turbine (RWT) is employed in this study. The 10-MW RWT was developed in the Light Rotor project, in a cooperation between DTU wind energy and Vestas. Rotor blades were designed in this project and other structural components were determined by upscaling the NREL 5-MW reference wind turbine [18]. Table 1 summarizes the general

Table 1
Properties for the DTU 10-MW reference wind turbine [9].

Parameter	Value
Rating	10-MW
Type	Upwind/3blades
Control	Variable speed, collective pitch
Drivetrain	Medium speed, multiple stage gearbox
Cut in, rated and cut out wind speed (m/s)	4, 11.4, 25
Cut in, rated rotor speed (rpm)	6.0, 9.6
Rotor diameter (m)	178.3
Hub height (m)	119.0
Hub diameter (m)	5.6
Hub overhang (m)	7.1
Shaft tilt angle (deg)	5.0
Rotor precone angle (deg)	−2.5
Rotor mass (kg)	227962
Nacelle mass (kg)	446036
Tower mass[a] (kg)	628442

[a] : Mass for land-based tower in DTU wind energy report.

properties of the 10-MW RWT. Noted the tower mass in the Table 1 is for land-based concept and it was changed due to the modification on the tower to account for the connection with the floater, and to make the coupled tower natural frequencies outside the rotor excitation and thus to avoid the tower resonance. Further details of the 10-MW RWT is available in the DTU wind energy report written by Bak et al. [9].

In the present work, the 10-MW RWT is mounted on a semi-submersible floating platform with three catenary mooring lines. The floating structure was designed by Dr.techn. Olav Olsen AS [19] as part of the LIFES50+ project [20]. It consists of three outer columns, a central column, a star-shaped pontoon and a slab. The four columns are mounted on the star-shaped pontoon and the slab is attached at the bottom of the pontoon. The 10-MW semi-submersible FWT concept is illustrated in Fig. 1. Table 2 lists the main specifications of the OO-Star Wind Floater Semi 10-MW floating substructure.

The mooring system consists of three catenary mooring lines with equal pre-tension and with a horizontal angle of 120° between adjacent lines. Each line is connected to an outer column of the floating substructure through a fairlead correspondingly. A clump mass is applied to each line, which separate the line into two segments. The main specifications of the mooring system are listed in Table 3. The concepts of the floating substructure and the mooring system are presented in greater detail in the LIFES50+ project report [21].

Table 2
Properties for the OO-Star Wind Floater Semi 10-MW floating substructure [21].

Parameter	Value
Water depth (m)	130
Draft (m)	22
Main material	post-tensioned concrete
Overall mass (× 1000 kg)	21709
Displaced volume (m^3)	23509
Tower base interface above mean sea level (m)	11
Center of mass location below mean sea level (m)	15.255
Center of buoyancy location below mean sea level (m)	14.236
Roll and pitch inertia about center of mass (kg •m^2)	9.43×10^9
Yaw inertia about center of mass (kg •m^2)	1.63×10^{10}

Table 3
Properties for the OO-Star Wind Floater Semi 10-MW mooring system [21].

Parameter	Value
Initial vertical position of clump mass below MSL (m)	90.45
Initial radius to clump mass from centreline (m)	148.6
Anchor position below MSL (m)	130
Radius to anchors from platform centreline (m)	691
Mooring line length, clump mass upper segment (m)	160
Mooring line length, clump mass lower segment (m)	543
Equivalent mass per length in air (kg/m)	375.38
Equivalent weight per length in water (N/m)	3200.6
Extensional stiffness EA (N)	1.506×10^9

E: Young's modulus; A: cross sectional line area.

2.2. 10-MW drivetrain concept

A medium-speed drivetrain concept was initially proposed by DTU for the 10-MW RWT, but the parameters specified by DTU can only enable establishing a simplified drivetrain model, namely the single DOF torsional spring-damper system. To facilitate the research on the development of the 10-MW wind turbine drivetrain, a detailed drivetrain model was designed by Wang et al. [14,15,22], and sufficient design and dynamic modelling parameters were provided for public use. The drivetrian is designed as a four-point support configuration and integrates with a conventional three-stage gearbox.

Fig. 2 shows a schematic layout of the drivetrain, where the nomenclature of bearings is presented. Fig. 3 presents a topology of the drivetrain with the nomenclature of gears. In the first and the second planetary stages, ring gears are fixed on the gearbox housing, which is supported on the bedplate via torque arms. Input

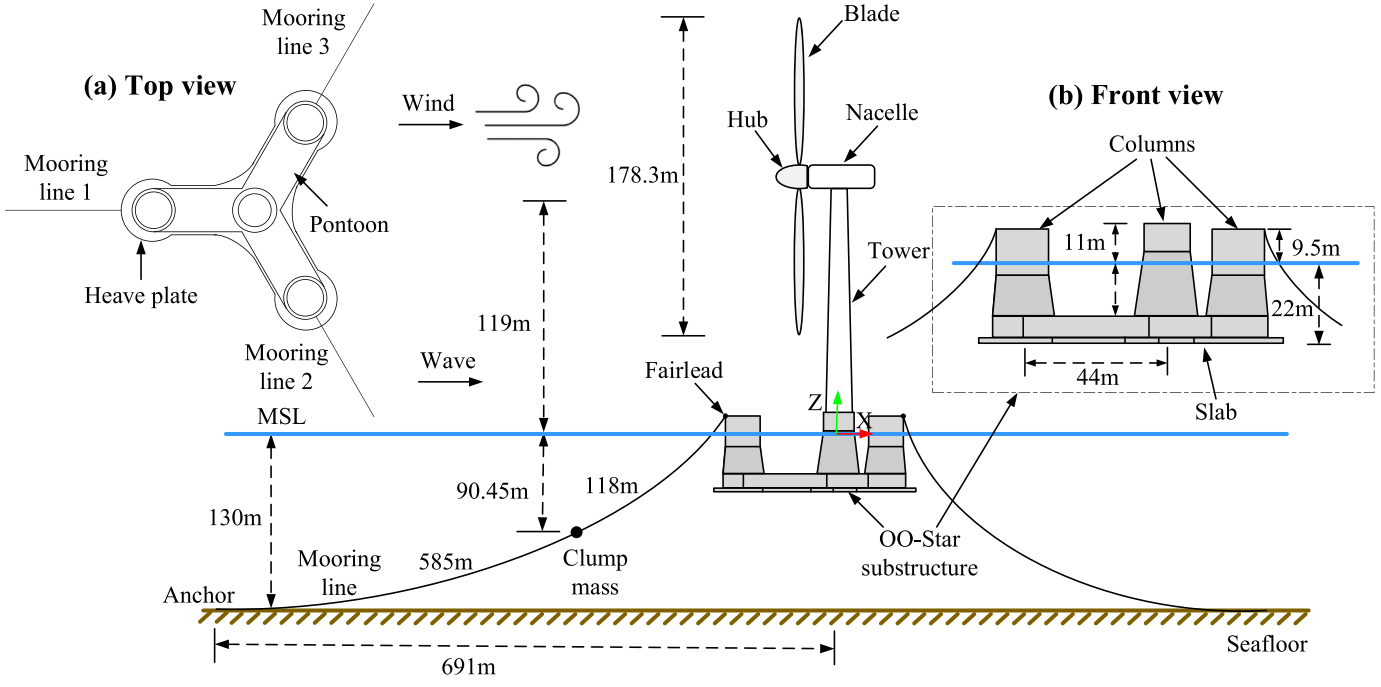

Fig. 1. Sketch of the OO-Star Wind Floater Semi 10-MW concept.

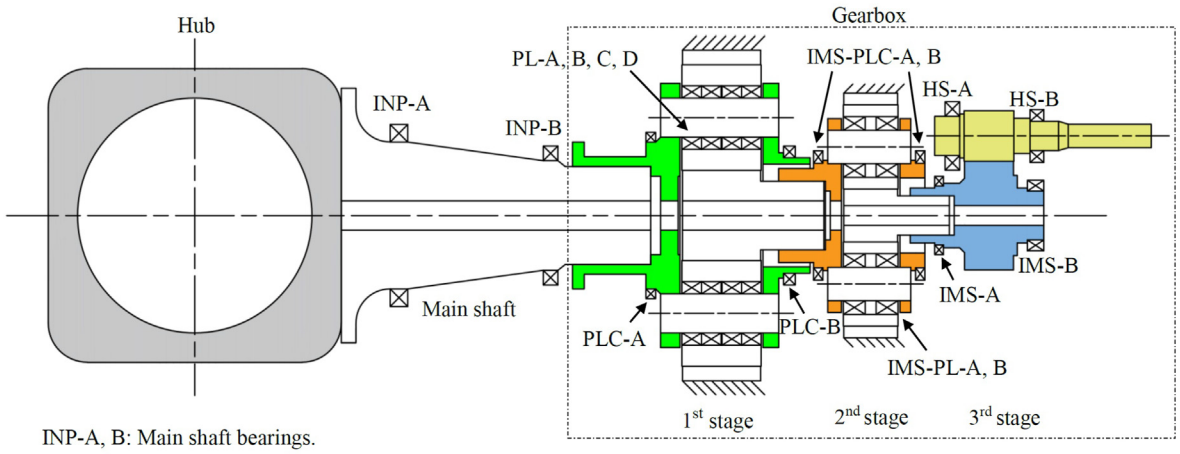

INP-A, B: Main shaft bearings.

PLC-A, B: Planet carrier bearing in the first stage; PL-A, B, C, D: Planet bearings in the first stage.

IMS-PLC-A, B: Planet carrier bearing in the second stage; IMS-PL-A, B: Planet bearings in the second stage.

IMS-A, B: Intermediate shaft bearings in the third stage; HS-A, B: High speed shaft bearings in the third stage.

Fig. 2. 10-MW wind turbine drivetrain schematic layout [14].

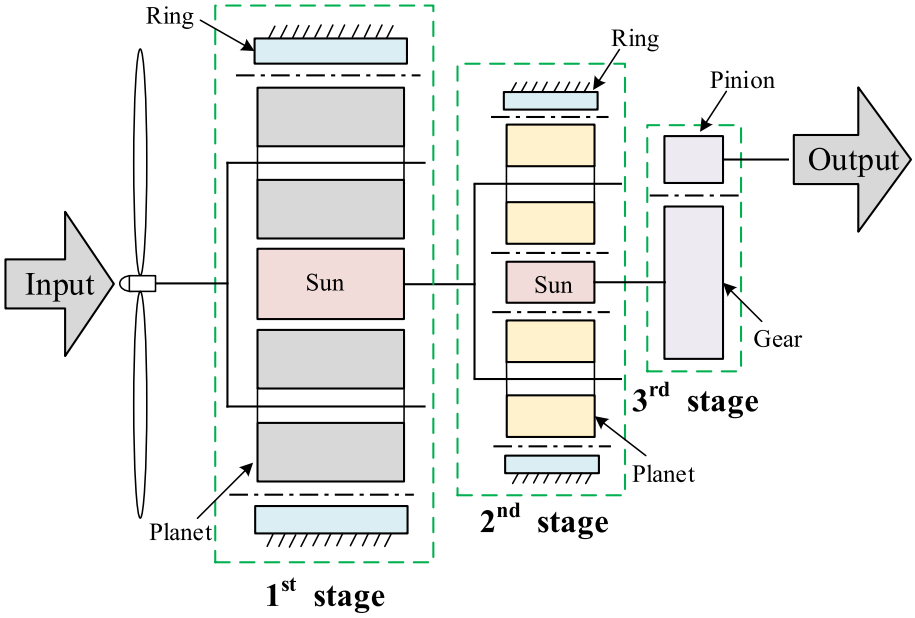

Fig. 3. 10-MW wind turbine drivetrain topology.

torque is applied on the planet carriers and sun gears serve as the output torque. In the third parallel stage, torque is delivered from the sun gear of the second planetary stage to generator through the gear pair (Gear-Pinion) in the high-speed stage. Hereby the rotation energy is transformed from the low-speed and high-torque to high-speed and low-torque form, and the conversion of mechanical energy to electric energy is realized.

The drivetrain bearings and gears were designed based on fatigue limit state (FLS) design criteria, while bedplate was designed based on the ultimate limit state (ULS) criteria according to relevant wind turbine international design standards. Main specifications of the drivetrain are given in Table 4. More details about the drivetrain concept is documented in the studies of Wang et al. [14,15,22].

3. Analysis methodology

3.1. Fully coupled analysis method

This section presents a fully coupled aero-hydro-servo-elastic analysis method for time domain dynamic analysis of the wind turbine drivetrain. An overview of the methodology is illustrated in Fig. 4. The fully coupled method is realized via a multi-body system (MBS) simulation tool, Simpack [23]. Compared to the conventional wind turbine dynamic model that considers drivetrain as a single DOF spring-damper system, the simulation tool is capable of modelling a high-fidelity drivetrain. Additionally, it integrates three separate codes: AeroDyn [24], HydroDyn [25] and Matlab/Simulink,

Table 4
10-MW wind turbine drivetrain specifications [14].

Parameter	Value
Drivetrain type	Four-point support
Gearbox type	Two planetary + one parallel
First stage ratio	1:4.423
Second stage ratio	1:5.192
Third stage ratio	1:2.179
Total ratio	1:50.039
Rated input shaft speed (rpm)	9.6
Rated generator shaft speed (rpm)	480.4
Rated input shaft torque (kN·m)	9947.9
Rated generator shaft torque (kN·m)	198.8
Gearbox dry mass (× 1000 kg)	60.43
Bedplate dry mass (× 1000 kg)	102.39
Maximum gear outer diameter (m)	3.098
Gearbox length (m)	5.964
Designed service life (year)	20

Table 5
Eigenmodes and eigenfrequencies of the 10-MW fully coupled rotor-drivetrain-bedplate-tower model.

Mode	E_freq. (Hz)	Mode description
1	1.528	Blade out-of-plane bending and drivetrain vertical bending
2	1.532	Blade out-of-plane bending and drivetrain horizontal bending
3	1.884	Blade in-plane bending and drivetrain torsion
4	3.226	Blade in-plane bending and drivetrain torsion
5	3.805	Blade out-of-plane bending, tower forth-back bending and drivetrain and bedplate vertical bending
6	4.148	Two blade out-of-plane bending and one blade in-plane bending, tower side-side bending, drivetrain horizontal bending and bedplate torsion
7	4.416	Two blade out-of-plane bending, tower side-side bending, drivetrain horizontal bending and bedplate torsion
8	4.612	Blade out-of-plane bending, tower forth-back bending, and drivetrain and bedplate vertical bending
9	6.105	Blade in-plane bending and drivetrain torsion

which accounts for wind turbine aerodynamics, hydrodynamics and control system dynamics, respectively. The gear and bearing load effects are calculated by the wind turbine fully coupled simulations. A computational flowchart of the fully coupled dynamic analysis method is illustrated in Fig. 5. More detailed introduction to dynamics for each module in the fully coupled analysis method is given in the following sections.

3.1.1. Aerodynamics

The aerodynamic loads on the rotor blades are calculated by a time-domain wind turbine aerodynamic module AeroDyn, which was developed by NREL and has been coupled to Simpack to carry out the aero-elastic simulations of horizontal axial wind turbines. Wind input to AeroDyn is generated by a three-dimensional stochastic inflow turbulence tool, TurbSim [26], where the Kaimal turbulence model is considered. The instantaneous position, orientation and velocities of wind turbine structure in Simpack are provided to AeroDyn and then AeroDyn calculates the aerodynamic loads on airfoils, which are then returned back to Simpack. The aerodynamic loads on the rotor blades are calculated based on Blade-Element/Momentum (BEM) method with various advanced corrections. More specifically, the Prandtl correction is implemented in the tip- and hub-loss models to account for the vortex shedding; the Glauert correction is used to account for large induced velocities (induction factor is greater than 0.4); the skewed wake correction is considered based on dynamic inflow method of Pitt and Peters, to account for the effects of skewed inflow; a semi-empirical Beddoes-Leishmann model is applied to account for the dynamic stall effects. The dynamic wake effect is not considered in the AeroDyn-BEM method. A detailed description of the BEM method used in this study is documented in the AeroDyn Theory Manual [24]. Aerodynamic loads on the tower and nacelle are not included in the present work.

3.1.2. Hydrodynamics

Hydrodynamic loads on the 10-MW floating substructure are computed by another NREL simulation module HydroDyn, which is a time-domain hydrodynamics module and is coupled to Simpack to enable aero-hydro-servo-elastic simulations for offshore wind turbines.

In the HydroDyn, the hydrodynamic loads on the floating hull are calculated based on a combination of linear potential flow theory and Morison's equation. In the linear potential flow theory, the hydrodynamic loads are obtained by solving diffraction and radiation problems. The diffraction problem is used to obtain the wave excitation loads, which consist of Froude-Krylov and diffraction forces and moments; the radiation problem is dealt with to obtain added mass, potential damping and hydrostatic restoring loads. Viscous drag forces on the 10-MW floating substructure are incorporated through the drag term in the Morison's equation, where viscous drag coefficients for cylindrical columns of the floating substructure are estimated based on the Reynolds number and Keulegan-Carpenter number and detailed parameters are given in the LIFES50+ project reports [2,27]. Hydrodynamic coefficients, namely the added mass and potential damping coefficients as well as first-order wave excitation load transfer function are firstly estimated in the frequency domain by a panel model in WAMIT [28]. These hydrodynamic coefficients are then applied in the time domain using a hybrid frequency-time domain approach that was initially introduced by Cummins [29].

The time-domain motion equation of the floating hull is written as below, which is solved in Simpack where the floating platform is considered as a six-DOF rigid body.

$$(M + A_\infty)\ddot{x}(t) + \int_0^{\frac{\pi}{2}} k(t-\tau)\dot{x}(t)d\tau + Cx(t) = F_{exc}(t) \quad (1)$$

where M is the mass matrix of the floating platform, A_∞ is the added mass matrix at infinite frequencies, C is the restoring matrix, which consists of hydrostatic restoring matrix and non-linear restoring matrix from the mooring system. $k(t-\tau)$ is retardation function, which associates with fluid memory effects and can be found either by the frequency-dependent added mass or potential damping coefficient. $F_{exc}(t)$ is the excitation forces, which include the Froude-Krylov force, the diffraction force, the aerodynamic force and the non-linear viscous force.

At each coupling time step, HydroDyn receives the position, orientation, velocities and accelerations of the floating platform from Simpack, and then returns the radiation wave loads and the viscous forces calculated based on the motions as well as diffraction wave loads back to Simpack.

Second order wave forces and current are not included in the present work. Also, hydrodynamic loads on mooring lines are not considered in the Simpack model in this study.

3.1.3. Control system dynamics

The control system dynamics of the fully coupled wind turbine is carried out by co-simulation between the codes of Simpack and Matlab/Simulink. The co-simulation is performed via data exchange in the two simulation tools and data is updated and

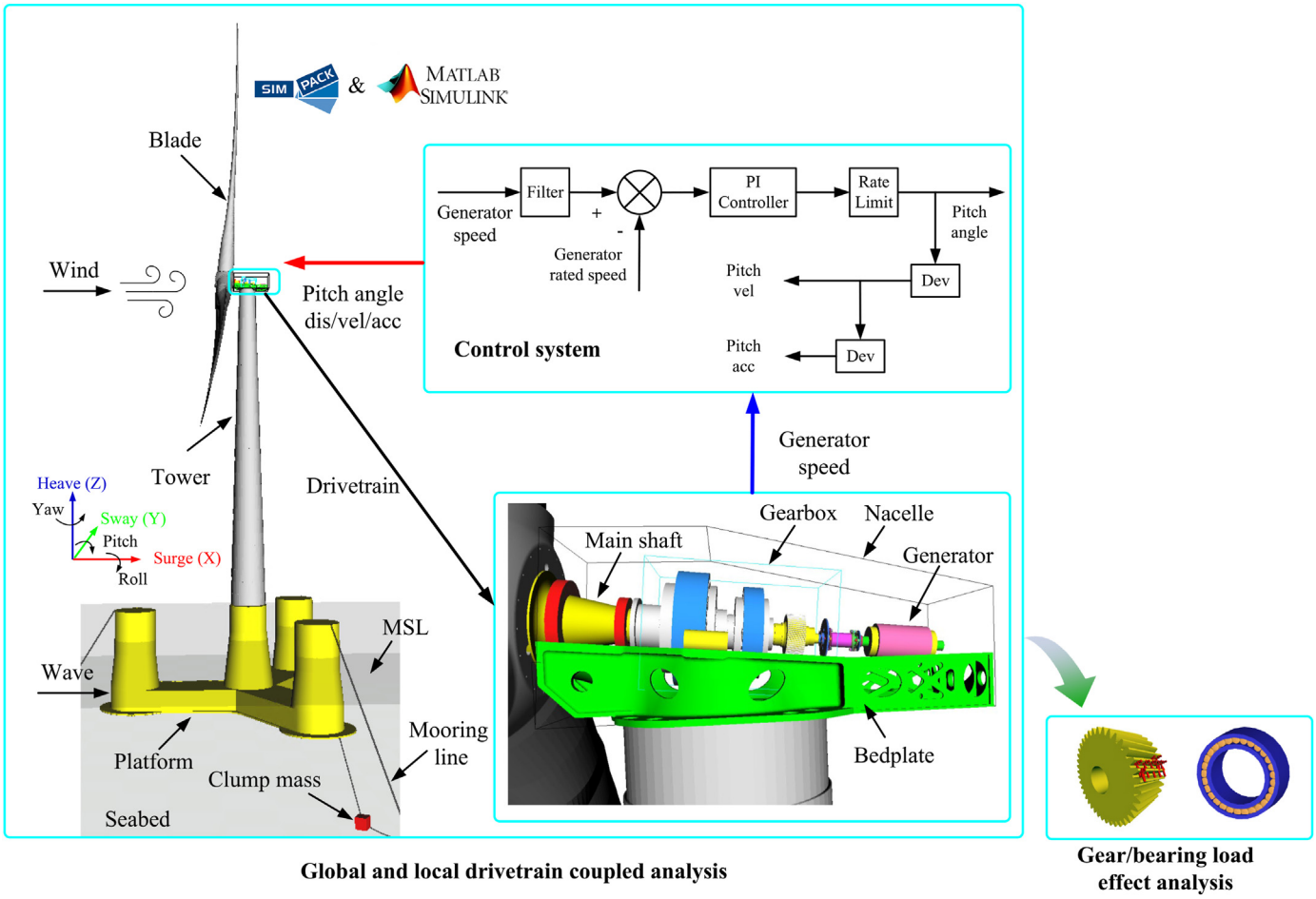

Fig. 4. Fully coupled method for wind turbine drivetrain analysis in a multi-body dynamic simulation tool.

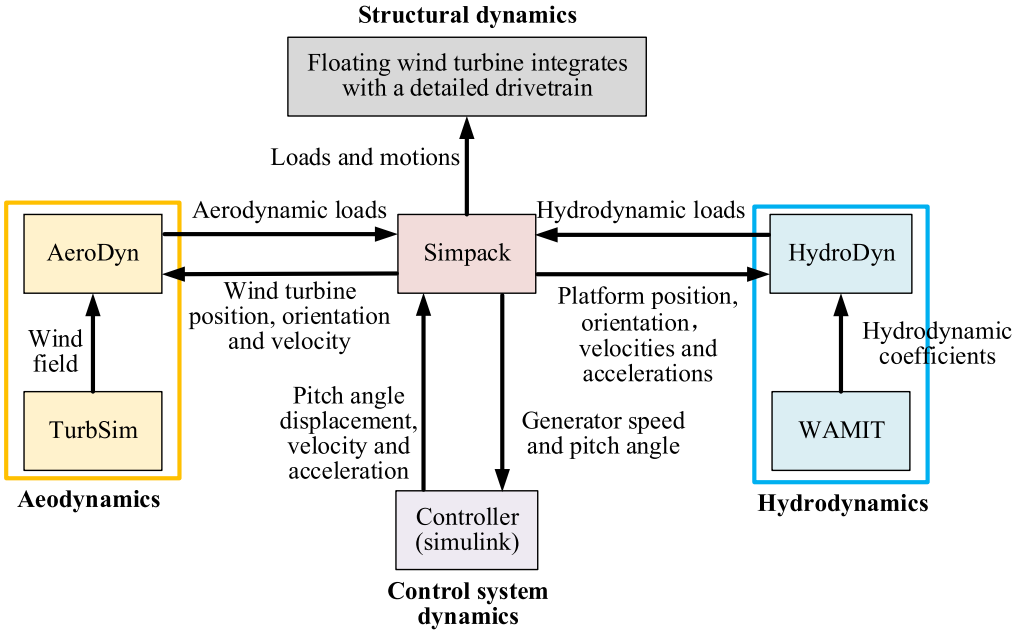

Fig. 5. Computational flowchart of fully coupled analysis method.

exchanged at each time step. The wind turbine dynamic model is established in Simpack and the blade pitch controller is defined in Matlab/Simulink. A simplified generator model is established in Simpack, which is represented by a torque-speed curve, as shown in Fig. 6. The generator torque-speed curve is obtained by a linear interpolation from dynamic simulation results of the 10-MW OO-Star Wind turbine model in Fast [30], an aero-hydro-servo-elastic numerical tool developed by the NREL, where the dynamic simulations are carried out in multiple wind speed conditions throughout from cut in to cut out. The blade pitch angle control is realized by a proportional-integral (PI) velocity controller. The objective of the PI controller is to minimize the error between the measured generator rotational speed from Simpack and the reference rotational speed shown in the Fig. 6. Based on this, the blade pitch angle is calculated via the following equation:

$$\beta = K_P(w_{mes} - w_{ref}) + K_I \int_0^t (w_{mes} - w_{ref})dt \quad (2)$$

where β is blade pitch angle; w_{mes} is the measured generator rotational speed that is obtained from Simpack; w_{ref} is the reference generator rotational speed that is rated speed as illustrated in Fig. 6; K_P and K_I are proportional and integral gains, respectively.

3.1.4. Structural dynamics and drivetrain resonance analysis

The wind turbine structural dynamics are solved based on the MBS method in Simpack, where rigid and flexible bodies are modelled and they are linked by means of joints and kinematic constraints. A reasonable structural modelling enables accurately describing its dynamic behaviour while ensuring an acceptable computational time. This study aims to get insight into the drivetrain dynamic behaviour in a global perspective. Based on this objective, critical components, blades, tower, main shaft and bedplate, are modelled as flexible bodies, and other components, such as gears and shafts inside the gearbox, are treated as rigid bodies. Blades are represented by flexible Euler-Bernoulli beam elements using a SIMBEAM module in Simpack, while other flexible bodies are modelled as reduced finite element bodies imported from ANSYS. Gear teeth contact is modelled by a specific force element FE225 in Simpack, which accounts for the gear teeth stiffness force, the damping force and the friction force. Gear teeth variable stiffness is calculated based on the international standard ISO 6336-1 [31]. Bearings are modelled with six-DOF linear diagonal stiffness and damping matrices. The coupling of bearing load effects between different DOFs and bearing clearances are not considered in this study. More details about the drivetrain dynamic model are presented in authors' previous work [14].

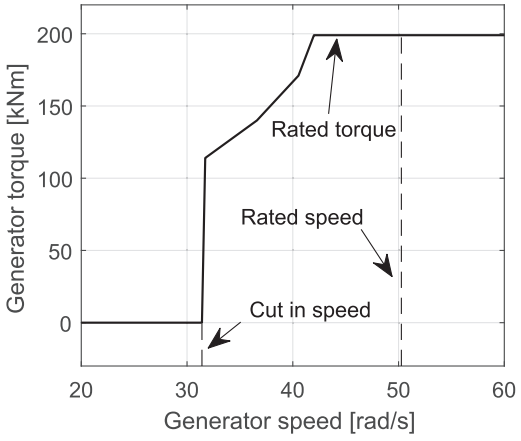

Fig. 6. 10-MW drivetrain generator torque-speed curve.

The mooring line model is also established based on the MBS method in Simpack. In the present work, each mooring line is divided into 21 segments for shape fitting. Each segment is modelled as a rigid cylindrical structure and the mass, moment of inertia in different DOFs and buoyancy are considered. Adjacent segments are connected by means of spring-damper elements, where the stiffness is calculated by Hooke's law. The mooring system modelling method adopted in this study refers to the study of Matha et al. [32], where a detailed description is given for a multi-body mooring system modelling in a FWT, and the feasibility of the modelling method is validated by the comparisons with the quasi-static results.

With the modelling of flexible blades and tower, eigenfrequencies of fully coupled rotor-drivetrain-bedplate-tower model would be much lower than those of the de-coupled drivetrain model, which renders the drivetrain at risk of resonance under low frequency environmental loading conditions. Thus, a resonance analysis of the drivetrain in the fully coupled wind turbine model is conducted. Table 5 lists the eigenmodes of the 10-MW fully coupled rotor-drivetrain-bedplate-tower model within 10 Hz and the first three eigenmodes are illustrated in Fig. 7. Since the focus of this study is on dynamics of the drivetrain, the eigenfrequencies that have no drivetrain shaking mode shape are not listed in this table.

The main eigenmodes of the fully coupled rotor-drivetrain-bedplate-tower model are composed of the blade in-plane or out-of-plane bending, the drivetrain horizontal or vertical bending or the drivetrain torsion, the bedplate vertical bending or torsion and the tower fore-back or side-side bending. In traditional drivetrain design and the associated dynamic analysis, only the first-order torsional eigenfrequency of drivetrains is analyzed to examine the risk of resonance due to the external loading excitation. However, in the 10-MW fully coupled model, it is observed that the first- and the second-order eigenfrequencies correspond to the drivetrain vertical and horizontal bending modes, respectively, and that they are lower than the drivetrain first-order torsional eigenfrequency. This implies that the risks of resonance of the drivetrain in the non-torsional directions are higher than that in the torsional direction under the excitation of the global loads. Therefore, attention should be paid to the non-torsional resonance check of drivetrains, especially for large-scale offshore wind turbines with large structural flexibility. Nevertheless, the lowest eigenfrequency in the fully coupled model is 1.528 Hz, which is still larger than the rotor 9P frequency: 1.440 Hz in rated and above conditions. Even if these estimates of natural frequencies are subjected to uncertainties, it seems that resonances of the drivetrain in the fully coupled model might be avoided.

3.2. De-coupled analysis method

In this section, the de-coupled method for the wind turbine driverain dynamic analysis is described, which is divided into three steps, as illustrated in Fig. 8. First, the global simulations of the wind turbine dynamic model are conducted using Simpack. In this global wind turbine model, the drivetrain is modelled in a simplified manner as a single DOF spring-damper system, because most of the widely used wind turbine simulation software, such as FAST, Bladed, SIMA, etc, consider drivetrain in this form. The simplified drivetrain consists of a main shaft, a generator shaft and a torsional spring-damper joint. The main shaft and the generator shaft are linked to a rigid bedplate with only one rotational DOF and the torsional moments of inertia of the rotor and the generator as well as drivetrain weight are considered. A drivetrain gear ratio of 1:50

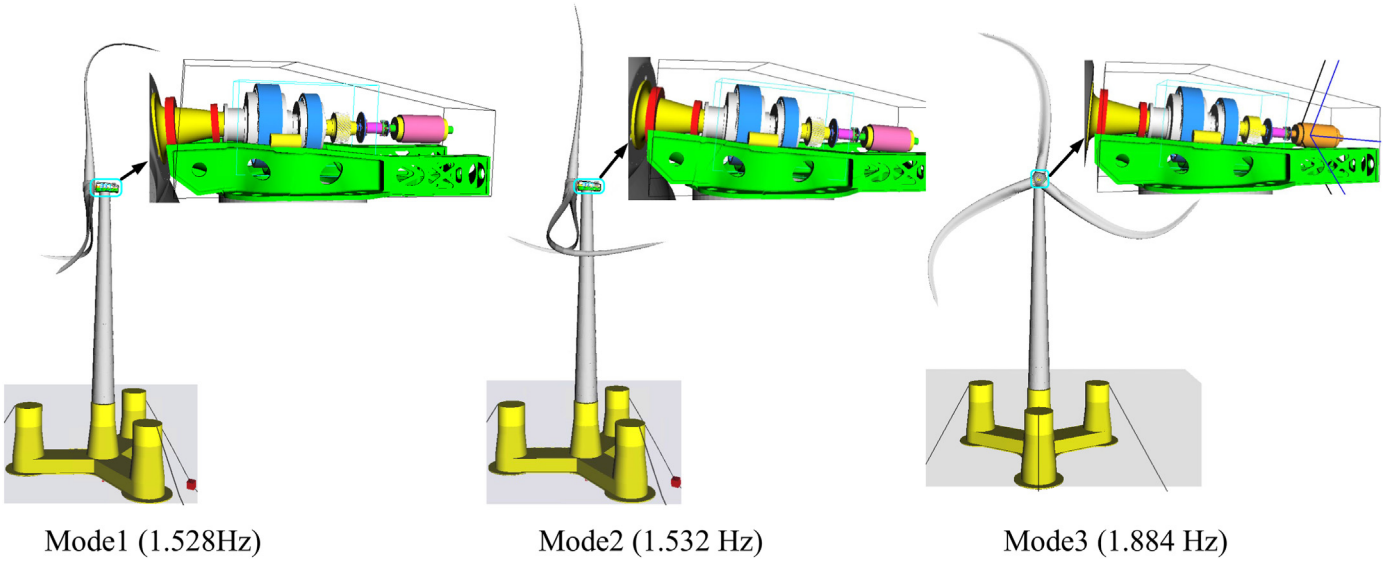

Fig. 7. The first three eigenmodes of the 10-MW fully coupled rotor-drivetrain-bedplate-tower model.

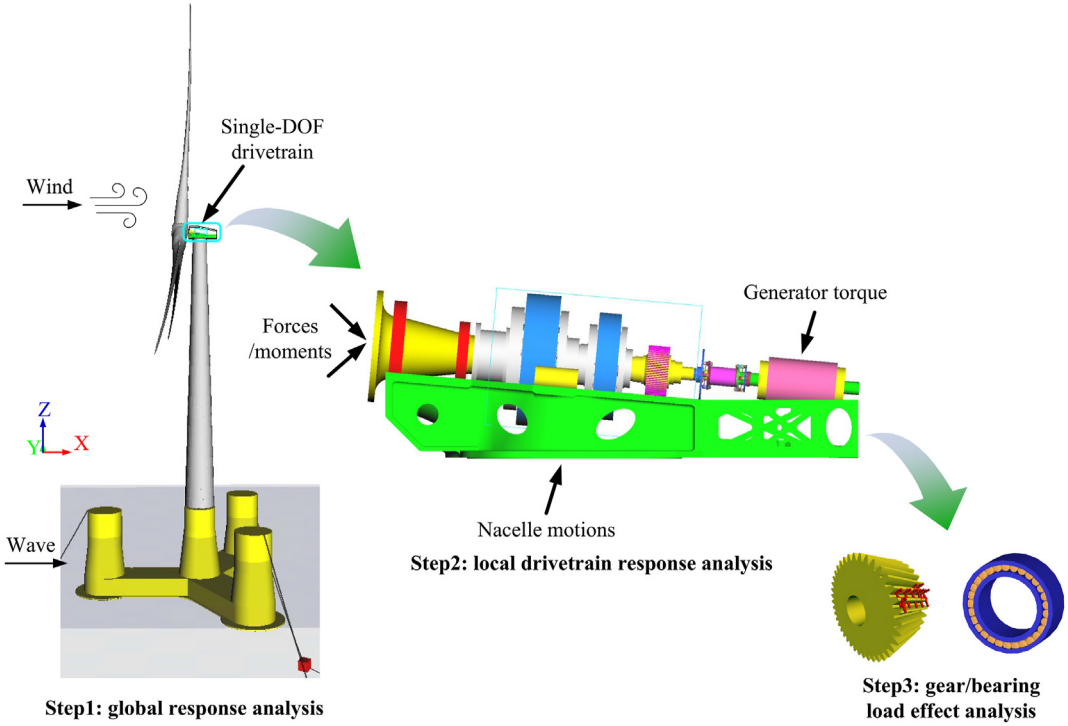

Fig. 8. De-coupled method for wind turbine drivetrain analysis.

is considered in the spring-damper joint. Then, the time series of loads and motions at the drivetrain boundary positions are extracted from the global analysis and are further used as input into the detailed drivetrain model in Simpack. More specifically, six-DOF input forces and moments in time domain are applied at the front end of the main shaft where the hub is connected. On the generator side, generator torque time series are applied at the generator shaft. The nacelle motions, represented by displacements, velocities and accelerations in time domain, are applied on the bottom of the bedplate, where yaw bearing is mounted. Finally, the gear and bearing load effects are calculated based on the local drivetrain analysis.

3.3. Fatigue damage calculation for bearings and gears

One-hour short-term fatigue damage of bearings and gears are addressed in the present work. Fig. 9 illustrates the process of creating bearing equivalent load distribution associated with cycles from load time series and load bins. First, the time series of bearing dynamic equivalent load P are calculated by the formula obtained from the international standard ISO 281 [33]:

$$P = XF_r + YF_a \tag{3}$$

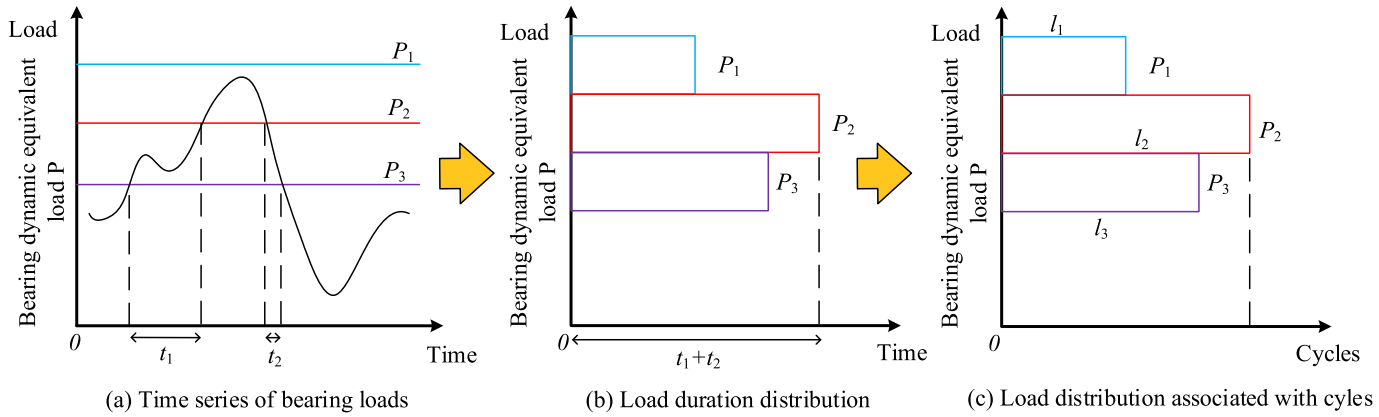

Fig. 9. Process of creating bearing equivalent load distribution associated with cycles from load time series and load duration distribution [15].

where F_r and F_a are time series of radial and axial loads of the bearing, respectively, obtaining from the MBS simulation. X and Y are dynamic loading factors that are obtained from the ISO 281 [33].

Then, load duration distribution (LDD) is created according to the method described by Nejad et al. [34], where the time series of bearing dynamic equivalent loads are divided into a number of load bins. Next, the LDD associates with time are transformed to LDD linked with cycle based on the formula [34]:

$$l_i = \sum_j \frac{t_j w_{bj}}{2\pi} \tag{4}$$

where l_i is the number of load cycles in the load bin i. t_j is the j-th time duration of the load bin i. w_{bj} is average bearing rotational speed (rad/s) in j-th time duration of the load bin i.

Next, the bearing basic rating life in each load bin is calculated based on the load-life relationship that is obtained from extensive experiments. The relationship is shown as follows [33]:

$$L_i = 10^6 \left(\frac{C}{P_i}\right)^a \tag{5}$$

where L_i basic rating life in the load bin i. L is defined as the number of cycles when 10% of the bearings supper pitting fatigue damage, while the other 90% of bearings are intact in one group test. C is the bearing basic dynamic load rating, which is a specific constant for one given bearing. a is the bearing life factor, for ball bearings, $a = 3$, and for roller bearings, $a = \frac{10}{3}$. Finally, the 1-h bearing fatigue damage is calculated based on the Palmgren-Miner linear accumulative damage hypothesis [35]:

$$D(EC) = \sum_i \frac{l_i(EC)}{L_i(EC)} = \frac{1}{C^a} \sum_i l_i(EC) \cdot P_i^a \tag{6}$$

where EC represents the environmental condition. $D(EC)$ is the 1-h accumulative bearing fatigue damage in the environmental condition EC. $l_i(EC)$ is the number of load cycles in the load bin i in the environmental condition EC. $L_i(EC)$ is the permissible number of cycles in the load bin i in the environmental condition EC. Gear teeth bending fatigue damage is estimated in this study. Similar to the procedure of calculating bearing fatigue damage, first, the time series of gear teeth bending stresses s is calculated based on the method in the gear standard ISO 6336-3 [36]. Then, gear teeth bending stress duration distribution (SDD) is created. Further, the SDD associated with time is transformed to that with cycle, where the number of gear teeth bending stress cycles in each stress bin is calculated via the following formula [34]:

$$n_i = \sum_j \frac{t_j w_{gj}}{2\pi} \tag{7}$$

where n_i is the number of stress cycles in the stress bin i. t_j is the j-th time duration of the bin i, and w_{gj} is the average gear rotational speed (rad/s) in the j-th time duration of the bin i. The sun and the ring gears mesh simultaneously with five and three planets in the first and the second stages, respectively, thus five and three times stress cycles are counted for the sun and the ring gears in the two planetary stages.

Finally, the 1-h gear teeth bending fatigue damage is calculated according to the Palmgren-Miner linear accumulative damage hypothesis [35]:

$$D(EC) = \sum_i \frac{n_i(EC)}{N_i(EC)} = \frac{1}{k} \sum_i n_i(EC) \cdot {s_i}^m \tag{8}$$

where $D(EC)$ is the 1-h accumulative gear teeth bending fatigue damage in the environmental condition EC, $n_i(EC)$ is the 1-h number of cycles in stress bin i in the environmental condition EC. $N_i(EC)$ is the permissible number of cycles in stress bin i in the environmental condition EC, which is calculated by the gear SN curve, namely, $N_i = k \cdot {s_i}^{-m}$, where k and m are SN curve parameters that are calculated based on international standards ISO 6336-3 [36] and ISO 6336-5 [37]. In the present thesis work, 200 load bins are used to calculate the 1-h bearing and gear fatigue damage in all cases. Greater details for the bearing and gear parameters are given in the studies of Wang et al. [14].

3.4. Environmental conditions and load cases

The 10-MW FWT is assumed to be installed at the Gulf of Maine site location with a water depth of 130 m. The description of environmental conditions at the site is provided in the LIFES50+ report [21]. Three load cases with turbulent wind and irregular wave are selected and used for the time domain dynamic simulations, as listed in Table 6. The wind and waves are considered to be directionally aligned, and current is not considered in this study. For each load case, five independent simulations with different wind and wave seeds are conducted to reduce the stochastic variations. Each simulation is carried out for 4000 s, and the first 400 s is removed to eliminate the start-up transient effects.

All the selected load cases are in the normal operating conditions, where the three mean wind speeds of 7.1, 13.9 and 22.1 m/s are represented as below, rated and above operating conditions. The corresponding waves, H_s and T_p, are the expected values for

Table 6
Load cases used for time domain dynamic simulations [38].

No.	Condition	u (m/s)	H_s (m)	T_p (s)	simulation time (s)
LC1	below	7.1	1.67	8.0	4000
LC2	rated	13.9	3.04	9.5	4000
LC3	above	22.1	6.20	12.5	4000

u: wind speed; H_s: significant wave height; T_p: wave spectral peak period.

given wind speed in the ocean site [21].

The normal wind profile model and normal turbulence model are considered in all of the load cases. The three-dimensional turbulent wind files are generated by using the TurbSim program using the Kaimal turbulence model applying for wind turbine Class C defined in the IEC 61400-1 [39]. The average wind speed u at the hub height of the 10-MW wind turbine is calculated using a power law profile with exponent 0.14, which is recommended in IEC 61400-3 [40]. The irregular Wave time series are generated by Pierson-Moskowitz spectrum with given H_s and T_p.

4. Results and discussions

4.1. Drivetrain model comparison

Wind turbine drivetrain is a complex combination of sub-components, including hub, main shaft, gearbox, generator coupling, electric generator and bedplate. The nonlinear dynamic coupling among these sub-components determines the complexity of the drivetrain dynamic behaviour, thus a high-fidelity modelling is required. An effective measure to assess whether the drivetrain dynamic model is reasonable, is to compare its first-order torsional eigenfrequency. First, the first-order torsional eigenfrequency of the drivetrain model is estimated by:

$$f = \frac{1}{2\pi}\sqrt{\frac{K}{I}} = \frac{1}{2\pi}\sqrt{\frac{\left[K_d^{-1} + (3K_b^{-1})\right]^{-1}(I_g \cdot R^2 + I_h + 3I_b)}{I_g R^2 \cdot (I_h + 3I_b)}} \tag{9}$$

where I is moment of inertia of the drivetrain in the torsional direction, which consists of the inertia of rotor (hub and blades) about the low speed shaft and the equivalent inertia of generator rotor at the low speed shaft. I_h is moment of inertia of hub. I_b is moment of inertia of blade about the low-speed shaft torsional axis. I_g is moment of inertia of generator rotor. R is reciprocal of the gear ratio of the drivetrain. K is the equivalent torsional stiffness of total drivetrain, which consists of torsional stiffness from hub to generator K_d, and equivalent blade torsional stiffness K_b at hub center.

The K_d is calculated by the following method. The generator rotor is set as fixed to bedplate and a static torque is applied at hub center. In order to get rid of the error caused by initial position of gear mesh, the torque is set as T_1 at the first time and T_2 at the second time. The angular position of the hub is α_1 under T_1 and α_2 under T_2. Based on this, the torsional stiffness of the drivetrain from hub to generator is calculated by:

$$K_d = \frac{T_2 - T_1}{\alpha_2 - \alpha_1} \tag{10}$$

The equivalent blade torsional stiffness K_b at hub center is calculated by:

$$K_b = (2\pi \cdot f_b)^2 \cdot I_b \tag{11}$$

where f_b is the first-order edgewise frequency of the blade.

All of the parameters and values that are used to calculate the first-order eigenfrequency of the drivetain model are listed in the Table 7 and the final result is calculated to be 1.964 Hz.

Then, using the numerical analysis method, the first-order eigenfrequencies of the simplified single-DOF and detailed drivetrain models are calculated based on the modal analysis in Simpack. The values and the modal shapes are illustrated in Fig. 10. The difference in the first-order eigenfrequency of the drivetrain calculated by the formula 9 and the detailed drivetrain numerical model is expressed as follows:

$$\text{Percentage difference} = \frac{|f_{numerical} - f_{formula}|}{f_{formula}} \times 100 \tag{12}$$

where $f_{formula}$ and $f_{numerical}$ are the first-order eigenfrequencies calculated by the formula 7 and the detailed drivetrain numerical model, respectively. The final result is calculated to be 4.07%, and the very small difference implies that the detailed drivetrain model is reasonably developed.

In addition, the difference in the first-order eigenfrequency for the single DOF and detailed drivetrain numerical models is expressed as follows:

$$\text{Percentage difference} = \frac{|f_{detailed} - f_{simplified}|}{f_{simplified}} \times 100 \tag{13}$$

where $f_{detailed}$ and $f_{simplified}$ are the first-order eigenfrequencies in the detailed and the single DOF drivetrain numerical models, respectively. The final result is calculated to be 7.47%. The small difference is due to that the moment of inertia of the gearbox components is neglected in the simplified drveitrain model. Yet, a good agreement between the simplified and the detailed drivetrain numerical models with respect to the first-order torsional eigenfrequency is still achieved.

4.2. Code-to-code comparison for the 10-MW floating wind turbine

Platform natural frequencies and dynamic responses of the 10-MW OO-Star FWT model are compared between the simulation codes: Simpack and Fast, which aims at validating whether the developed wind turbine dynamic model in Simpack could provide reasonable global response results. The 10-MW OO-Star wind turbine dynamic model in Fast was developed in the LIFES50+ project and detailed description is available in the report [27]. Identical AeroDyn and HydroDyn codes are employed in the two simulation tools. Moreover, identical environmental conditions, namely the

Table 7
Parameters and values of the simple drivetrain model.

Parameter	T_1 (kNm)	T_2 (kNm)	α_1 (rad)	α_2 (rad)	f_b (Hz)
Value	500	1000	1.523×10^{-3}	7.140×10^{-4}	0.948
Parameter	I_b (Kg · m^2)	I_h (Kg · m^2)	I_g (Kg · m^2)	R	I (Kg · m^2)
Value	5.592×10^7	3.257×10^5	1500.5	50.039	3.675×10^6
Parameter	K_d (Nm/rad)	K_b (Nm/rad)	K (Nm/rad)		
Value	6.177×10^8	1.984×10^9	5.596×10^8		

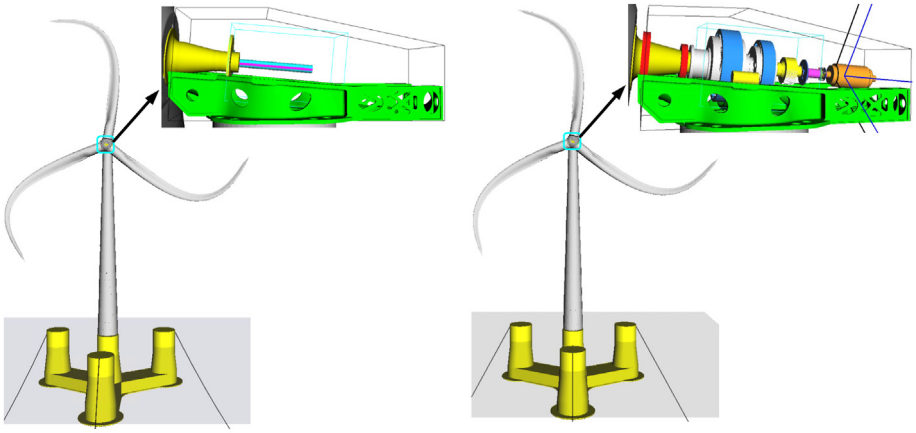

Fig. 10. The first-order eigenmodes of the simplified and detailed drivetrain models in Simpack.

turbulent wind and irregular waves are employed in the two software. Controller and mooring systems are different in the two models. Both pitch and generator control systems are used in the Fast model, while only pitch control is employed and the generator is modelled as a torque-speed curve in the Simpack model. In addition, in the Fast model, mooring system is developed by means of the MoorDyn [41] module using a lumped-mass approach, and hydrodynamic loads on mooring lines are taken into account; as a comparison, in the Simpack model, a multi-body system approach is employed to establish mooring lines and hydrodynamic loads on the mooring lines are not considered.

4.2.1. Platform natural frequency

Decay simulations of the 10-MW FWT are carried out in the two simulation codes. Identical initial displacements in surge, heave, pitch and yaw directions are placed at the floating platform in the Simpack and Fast models. Then, the wind turbine systems are left to oscillate and decay until reaching the equilibrium position. Time series of free decay in the four DOFs are converted to frequency domain by the Fourier transform, thereby obtaining the natural frequencies of the FWT system. Table 8 compares the decay simulation results for the FWT system between the Simpack and Fast codes. The comparison is expressed as follows:

$$\text{Percentage difference} = \frac{|f_{Simpack} - F_{Fast}|}{f_{Fast}} \times 100 \tag{14}$$

where $f_{Simpack}$ and f_{Fast} are the natural frequencies of the wind turbine system from decay simulations in Simpack and Fast codes, respectively.

While small percentage differences of the system natural frequency exist in the surge direction, which is due to the difference in the mooring line stiffness in the two models, the results calculated in the Simpack model generally accord well with those from the Fast model.

Table 8
Comparison of system natural frequencies from decay simulations.

Free decays	Surge	Heave	Pitch	Yaw
Fast	0.0054	0.0478	0.0316	0.0097
Simpack	0.0050	0.0483	0.0320	0.0100
% difference	7.41	1.05	1.27	3.09

4.2.2. Forced dynamic response

In this section, time-domain dynamic responses of the 10-MW FWT models developed in Fast and Simpack are compared. Since the wind turbine model in Fast employs the single-DOF drivetrain, the simplified single-DOF drivetrain is also used in the wind turbine model in Simpack, which is to avoid the possible influence of the detailed drivetrain on global analysis.

The power generation, tower top loads, nacelle acceleration and blade pitch angle from the two codes are compared in this study, because they are closely related to the drivetrain dynamic performance. Figs. 11–14 present these time domain comparisons in different environmental conditions. The results indicate that these global dynamic responses of the wind turbine model obtained from the two codes agree well. Hence, the developed wind turbine dynamic model in Simpack is found to give reasonable results.

4.3. Comparison of drivetrain dynamic behaviour in fully coupled and de-coupled models

In this section, drivetrain dynamic behaviour in the fully coupled and de-coupled models are compared. The comparison is expressed by percentage difference, χ, of 1-h fatigue damage of bearings and gears for the fully coupled and de-coupled models, defined as:

$$\chi = \frac{D_{de} - D_{full}}{D_{full}} \times 100 \tag{15}$$

where D_{full} and D_{de} represent the 1-h fatigue damage of bearings and gears calculated in the fully coupled and the de-coupled models, respectively.

One-hour fatigue damage of bearings and gears in the fully coupled and de-coupled models are compared under below-rated, rated and above-rated conditions. Under each load case, identical wind and waves sample are used for the fully coupled and de-coupled analysis. The percentage differences of the 1-h fatigue damage calculated based on Eq. (15) are listed in Table 9. The sequence of bearings and gears displayed in the figure is based their locations in the drivetrain, from the rotor to the generator side. Additionally, the nomenclature of bearings and gears in the figure corresponds to that presented in Figs. 2 and 3, respectively. It is found that fatigue damage of drivetrain bearings and gears calculated using the de-coupled method is generally very close with that calculated by the fully coupled method. Under the above-rated

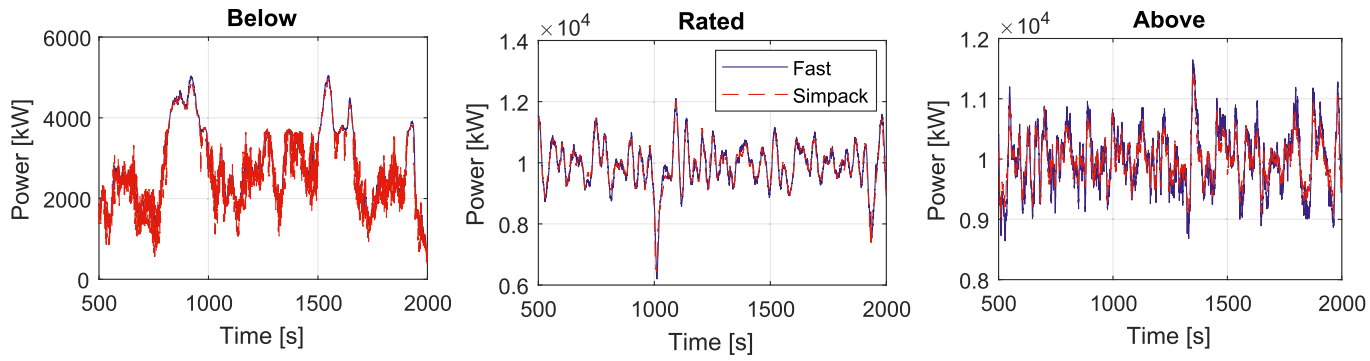

Fig. 11. Comparison of power generation in Fast and Simpack for each wind speed condition.

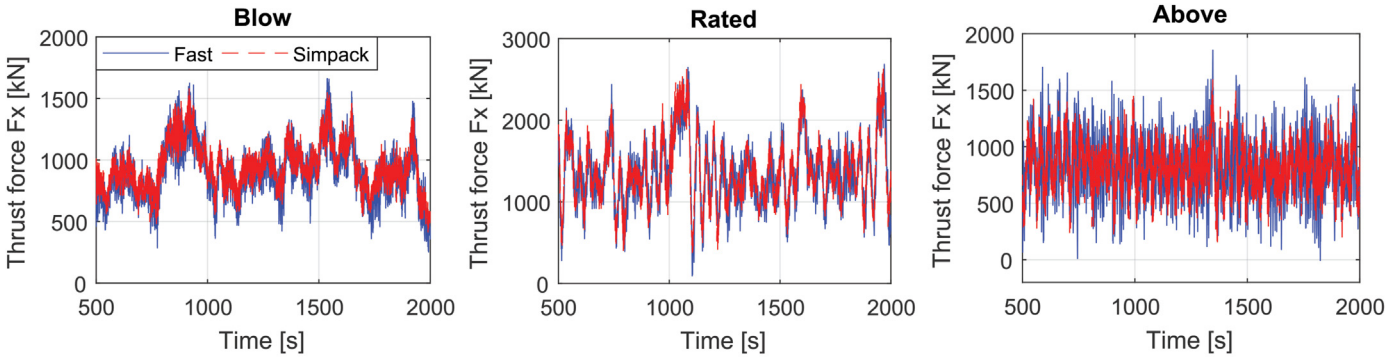

(a) Thrust force Fx

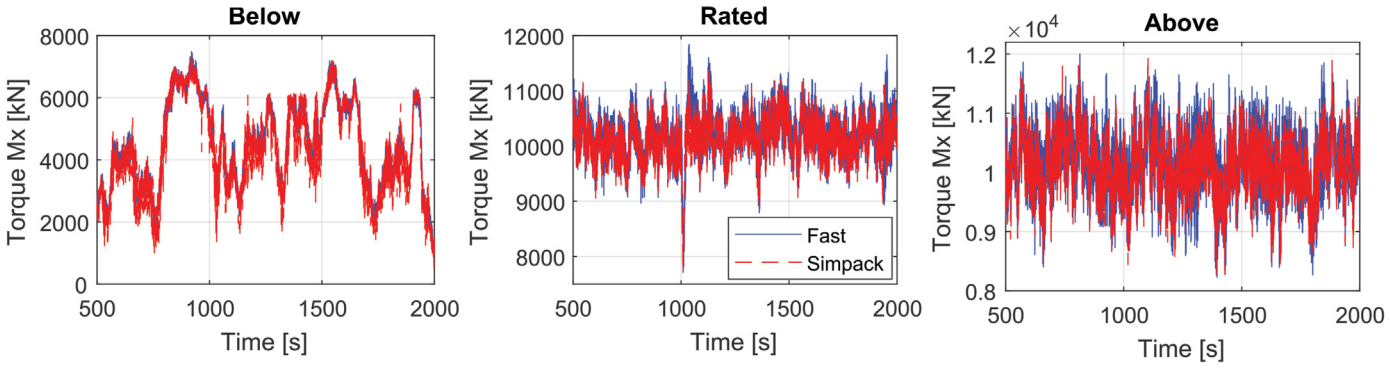

(b) Torque Mx

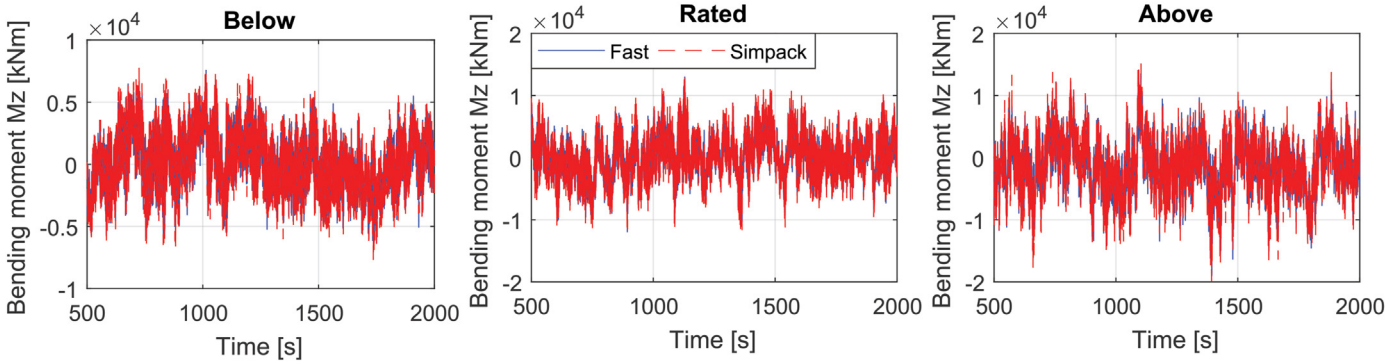

(c) Bending moment Mz

Fig. 12. Comparison of tower top loads in Fast and Simpack for each wind speed condition: (a) thrust force; (b) torque; (c) bending moment.

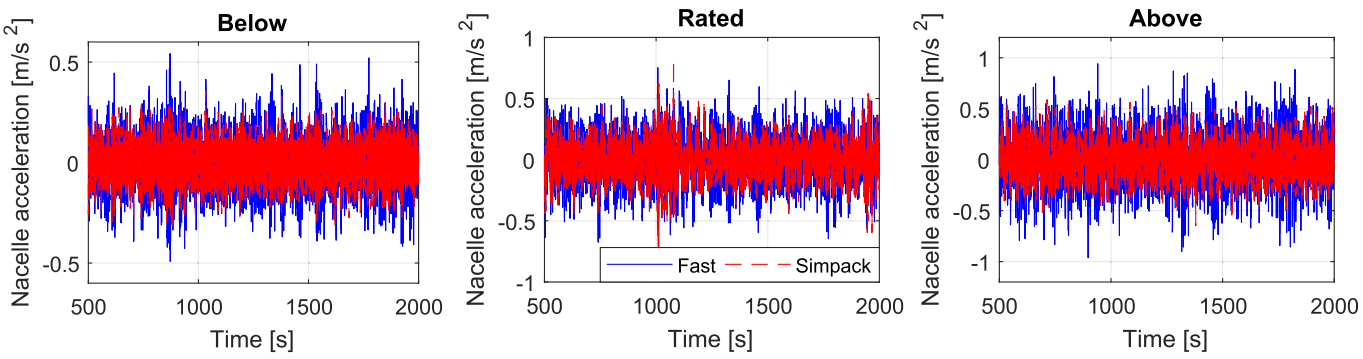

Fig. 13. Comparison of nacelle acceleration in wind speed direction in Fast and Simpack for each wind speed condition.

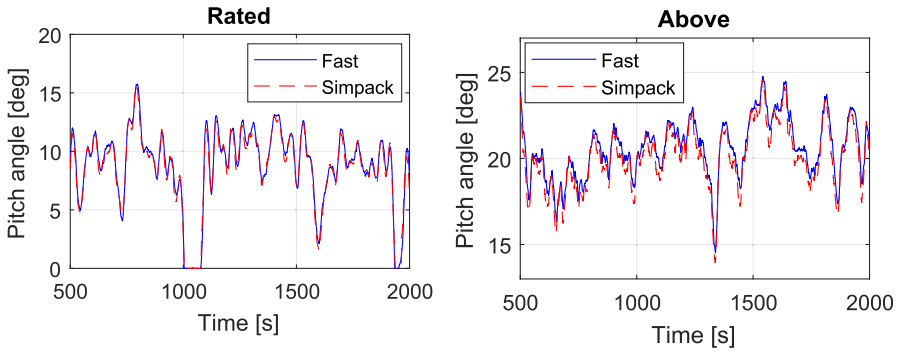

Fig. 14. Comparison of blade pitch angle in Fast and Simpack for each wind speed condition.

Table 9
Comparisons of fatigue damage of bearings and gears in fully coupled and de-coupled models.

Components	%difference of 1-h fatigue damage		
	Below-rated	Rated	Above-rated
INP-A	−1.174%	−1.391%	5.470%
INP-B	−2.645%	−2.764%	6.545%
PLC-A	−0.020%	0.279%	0.087%
PLC-B	0.041%	−5.420%	−5.749%
IMS-PLC-A	0.995%	−0.548%	−1.128%
IMS-PLC-B	0.104%	0.073%	−1.153%
IMS-A	0.752%	0.304%	−1.173%
IMS-B	0.107%	−0.290%	−0.956%
HS-A	−0.101%	0.094%	−1.121%
HS-B	0.173%	0.013%	−1.101%
1st Sun	−0.048%	−0.035%	−2.488%
2nd Sun	0.152%	−0.070%	−2.423%
3rd Pinion	0.122%	0.054%	−2.026%

condition, fatigue damage in main bearings INP-A and INP-B are slightly higher in the de-coupled model than that in the fully coupled model. By contrast, fatigue damage in bearing PLC-B is slgihtly lower in the de-coupled model than that in the fully coupled model under the rated and above-rated conditions. Under the below-rated condition, for all of the bearings and gears, the percentage differences in fatigue damage calculated by the fully coupled and de-coupled methods are less than 3%.

Fig. 15 compares the load effects of the bearing INP-A in time- and frequency-domain for the fully coupled and de-coupled models under the above-rated condition. The fatigue damage of the bearing INP-A is determined by its radial forces, thus only forces of Fy and Fz are analyzed. The responses refer to a non-rotational coordinate system at the bedplate and the vector directions of the coordinate axes are shown in Fig. 4. In general, very close load effects of the main bearing INP-A in the fully coupled and de-coupled models are observed. Fluctuations in the force time series of Fy and Fz of the bearing INP-A are induced by the low-frequency turbulent wind induced response as well as rotor 3P, 6P and 9P responses, which is revealed by the load spectra. The main bearing load effects are mainly determined by the drivetrain shaft bending moments obtained from global simulations, thus it implies that the detailed drivetrain model will make very limited influence on the wind turbine global dynamic responses.

The results presented in Table 9 under each load case are based on a single wind and wave sample. Different numbers of wind and wave samples used for wind turbine global simulations would lead to different absolute fatigue damage in drivetrain bearings and gears. Effect of uncertainty of the number of wind and wave samples on 1-h fatigue damage of bearings and gears of the 10-MW drivetrain was investigated in the authors' another study [42], which shows that the largest deviation of the drivetrain fatigue damage caused by the number of samples is less than 5%; when five samples are used for simulations, the deviations in the fatigue damage of the main bearings and the gearbox bearings are less than 2% and 1%, respectively.

It is interesting to check whether or not different samples would make the percentage difference, not the absolute value, of the 1-h fatigue damage between the fully coupled and de-coupled analysis a big difference. In order to clarify this, the percentage differences in the drivetrain 1-h fatigue damage in different wind and wave samples are compared under the above-rated condition, as presented in Table 10. Since this study focus on the comparison of fully coupled and de-coupled methods for drivetrain simulations, identical wind and wave seeds are used in each case for the fully coupled and de-coupled simulations. It is observed that the

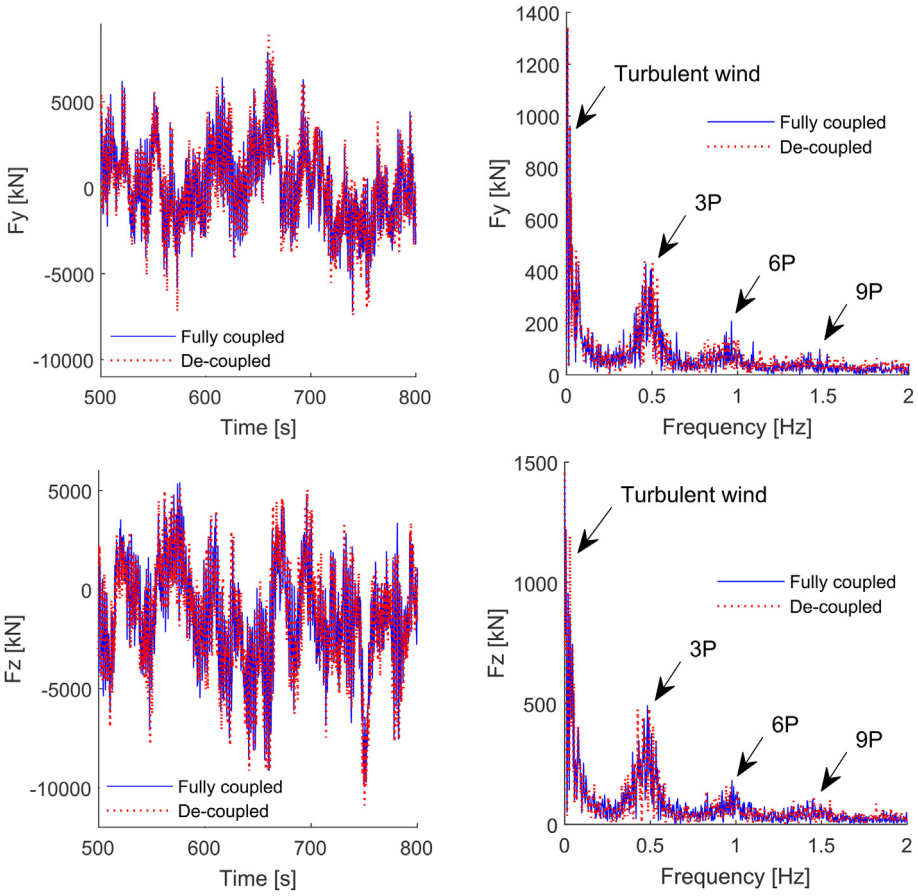

Fig. 15. Comparison of load effects of bearing INP-A in time- and frequency-domain in fully coupled and de-coupled models under the above-rated condition.

Table 10
Comparisons of percentage difference in fatigue damage of bearings and gears in fully coupled and de-coupled models in different wind and wave samples under the above-rated condition.

Components	%difference of 1-h fatigue damage					
	Sample1	Sample2	Sample3	Sample4	Sample5	Mean value
INP-A	5.470%	−0.260%	2.592%	2.772%	−0.037%	2.107%
INP-B	6.545%	1.444%	2.768%	3.546%	0.644%	2.989%
PLC-A	0.087%	−0.017%	0.359%	−0.011%	0.211%	0.126%
PLC-B	−5.749%	−5.875%	−5.364%	−6.001%	−5.907%	−5.779%
IMS-PLC-A	−1.128%	−1.300%	−0.842%	−1.479%	−1.060%	−1.162%
IMS-PLC-B	−1.153%	−1.166%	−0.705%	−1.236%	−0.974%	−1.047%
IMS-A	−1.173%	−1.237%	−0.479%	−1.301%	−0.913%	−1.021%
IMS-B	−0.956%	−1.015%	−0.523%	−1.208%	−0.923%	−0.925%
HS-A	−1.121%	−1.233%	−0.680%	−1.325%	−0.951%	−1.062%
HS-B	−1.101%	−1.063%	−0.621%	−1.169%	−0.848%	−0.961%
1st Sun	−2.488%	−2.482%	−2.329%	−2.754%	−2.432%	−2.497%
2nd Sun	−2.423%	−2.484%	−2.428%	−2.660%	−2.332%	−2.466%
3rd Pinion	−2.026%	−2.176%	−1.942%	−2.358%	−2.015%	−2.103%

percentage differences of main bearings INP-A and INP-B between the fully coupled and de-coupled models are obviously different in different wind and wave samples, while very small changes are seen on the gearbox bearings and gears. This implies that different wind and wave samples will affect the comparison results of the fully coupled and de-coupled models on main bearings, but not on the bearings and gears in the gearbox. This is because different samples mainly lead to different global non-torque loads, which dominate the fatigue damage of main bearings, while bearings and gears in the gearbox are dominated by torque loads, which are slightly affected by different samples due to the control effect. From the Table 10, it is seen that the mean values of percentage differences of 1-h fatigue damage in main bearings INP-A and INP-B over five independent samples are less than 3%, which indicates that de-coupled method will cause very small effects on main bearing fatigue damage. Note that since the absolute fatigue damage of the bearing PLC-B is quite low, which makes it sensitive to the changes in gear teeth mesh force, thus the slightly larger percentage difference in Table 10 does not influence its required service life.

As a whole, the de-coupled analysis method could generally provide accurate results for drivetrain dynamic analysis as predicted by the fully coupled analysis method. Therefore, the de-

Table 11
Comparisons of 1-h fatigue damage of bearings and gears between the conditions of with and without nacelle motions in the de-coupled analysis.

Components	%difference of 1-h fatigue damage		
	Below-rated	Rated	Above-rated
INP-A	0.501%	1.057%	0.580%
INP-B	0.417%	0.865%	0.508%
PLC-A	−5.819%	−8.722%	−5.345%
PLC-B	2.988%	3.644%	2.050%
IMS-PLC-A	−3.009%	−1.544%	−1.181%
IMS-PLC-B	−5.239%	−3.498%	−2.143%
IMS-A	0.421%	0.722%	0.376%
IMS-B	1.033%	0.979%	0.487%
HS-A	0.812%	1.020%	0.614%
HS-B	−0.194%	0.301%	0.193%
1st Sun	0.631%	0.818%	0.484%
2nd Sun	0.583%	0.929%	0.339%
3rd Pinion	0.623%	0.861%	0.415%

coupled method could be confidently used if the resonance does not appear in the drivetrain in the fully coupled wind turbine system.

4.4. Effect of nacelle motions in the de-coupled analysis

In the current wind industry, the de-coupled method is usually employed for drivetrain design. Wind turbines and drivetrains are usually designed by different engineering companies, where one party designs rotor, tower and foundation and another party designs the drivetrain. In the drivetrain design, usually only design loads are used without considering the nacelle motions. This is mainly because that current widely used drivetrain design software is unable to consider time-domain nacelle motions, thus the drivetrain is usually designed under the condition that the bedplate is fixed. This method could be applicable for the traditional drivetrain design, which is generally for land-based or fixed offshore wind turbines, where nacelle motions are quite small, making negligible effect on drivetrain fatigue damage. However, in the floating offshore wind turbines, nacelle motions are much larger and very dependent on different floating support structures. It is a question whether the nacelle motions could still be ignored in the drivetrain design for FWTs and if ignored, whether it leads to a conservative or non-conservative design.

In order to shed light on this question, effect of nacelle motions on drivetrain fatigue damage in the de-coupled analysis is studied. Drivetrain fatigue damage between the conditions of with and without nacelle motions are compared. The comparison is expressed by percentage difference, χ, of 1-h fatigue damage of bearings and gears for the without and with motion conditions, defined as:

$$\chi = \frac{D_{without} - D_{with}}{D_{with}} \times 100 \tag{16}$$

where D_{with} and $D_{without}$ represent the 1-h fatigue damage of bearings and gears calculated in the conditions of with and without motions, respectively, in the de-coupled analysis.

Table 11 lists the comparisons of the 1-h fatigue damage of bearings and gears of the drivetrain between conditions of with and without nacelle motions under the three load cases. When the nacelle motions are not considered in the de-coupled analysis, fatigue damage in the upwind planet carrier bearing PLC-A (as demonstrated in Fig. 2) in the first planetary stage is clearly lower under all of the load cases than that in the condition when the nacelle motions are considered. Under the below-rated condition, the planet carrier bearing IMS-PLC-B in the second planetary stage is slightly lower in the without motion condition than that in the with motion condition, but it would slightly contribute to the difference in the long-term fatigue damage, because the probability of occurrence of the low wind speed environmental conditions is small. Very small effect is found on other bearings and gears under all load cases.

In order to reduce the possible effect of statistical uncertainty, the comparisons are carried out in different wind and wave samples under the above-rated condition, as presented in Table 12. It is found that different samples lead to very limited effect on the comparison results for all of the bearings and gears between conditions of with and without nacelle motions and the bearing PLC-A is further identified as the most susceptible one to the nacelle motions.

To reveal the reason for the different fatigue damage in the bearing PLC-A, dynamic equivalent load distributions associated with cycles of the bearing between conditions of with and without motions are compared under the three load cases, as illustrated in Fig. 16. From the Figure (9) and Equation (6), it can be seen that fatigue damage of bearings depends on the bearing equivalent load P and load cycle l, where P plays a major role because of the power a, which is taken as $a = \frac{10}{3}$. From the Fig. 16, the bearing load cycles are close between the conditions of with and without motions under the three load cases, but the bearing equivalent loads are obviously larger under the with motion condition that those under the without motion condition, which serves as the main cause of the higher fatigue damage when the nacelle motions are considered.

Table 12
Comparisons of percentage difference in fatigue damage of bearings and gears between the conditions of with and without nacelle motions in different wind and wave samples under the above-rated condition.

Components	%difference of 1-h fatigue damage					
	Sample1	Sample2	Sample3	Sample4	Sample5	Mean value
INP-A	0.580%	0.586%	0.493%	0.502%	0.583%	0.549%
INP-B	0.508%	0.599%	0.508%	0.462%	0.542%	0.524%
PLC-A	−5.345%	−5.221%	−5.286%	−5.262%	−5.112%	−5.245%
PLC-B	2.050%	2.454%	2.378%	2.141%	2.315%	2.268%
IMS-PLC-A	−1.181%	−0.832%	−0.928%	−0.993%	−0.870%	−0.961%
IMS-PLC-B	−2.143%	−2.062%	−2.112%	−2.096%	−1.908%	−2.064%
IMS-A	0.376%	0.225%	0.396%	0.290%	0.466%	0.351%
IMS-B	0.487%	0.674%	0.595%	0.481%	0.634%	0.574%
HS-A	0.614%	0.675%	0.699%	0.672%	0.735%	0.679%
HS-B	0.193%	0.225%	0.162%	0.190%	0.255%	0.205%
1st Sun	0.484%	0.542%	0.517%	0.481%	0.588%	0.522%
2nd Sun	0.339%	0.699%	0.492%	0.465%	0.626%	0.524%
3rd Pinion	0.415%	0.521%	0.509%	0.494%	0.612%	0.510%

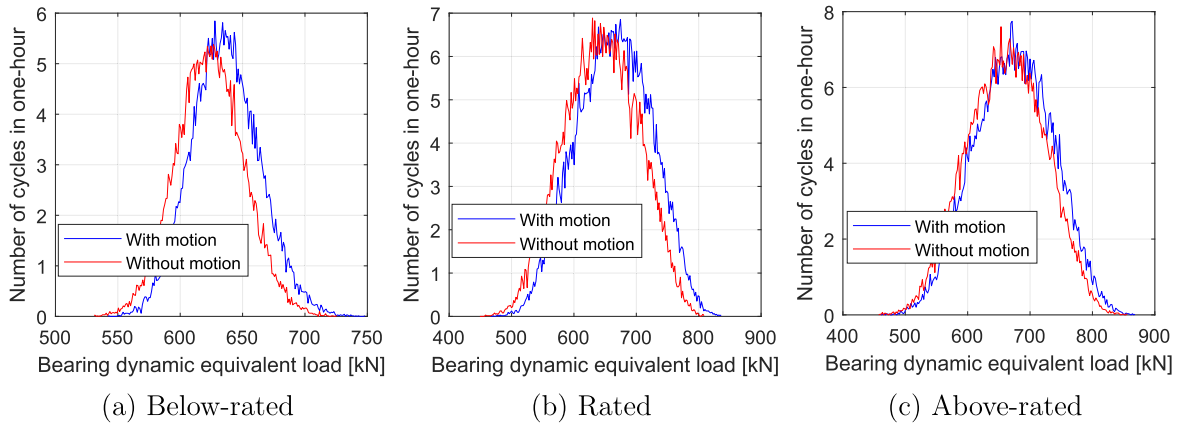

Fig. 16. Comparisons of bearing dynamic equivalent load (Eq. (3)) distribution associated with cycles (see Fig. 9) of bearing PLC-A in conditions of with and without nacelle motions, under below-rated, rated and above-rated load cases in the de-coupled analysis.

The dynamic equivalent load of the bearing PLC-A is calculated based on its axial force Fx and radial force Fr that consists of load components of Fy and Fz, as presented in Equation (3). Fig. 17 compares the mean values and standard deviations in each load component of the bearing PLC-A between conditions of with and without nacelle motions under the rated load case. Approximately same responses for the conditions of with and without nacelle motions are observed in radial forces Fy and Fz of the bearing PLC-A. By contrast, the main differences appear in the mean value and standard deviation of the axial force Fx, where higher responses are seen in the condition when the nacelle motions are considered. The higher mean value serve as the main reason for the higher fatigue damage in the condition of with nacelle motions because of the much higher amplitude than the standard deviation. The higher mean value of the axial force Fx of the bearing PLC-A is mainly cased by the axial component of the mass of the first planetary stage. The mass of the first planetary stage occupies a significant proportion over the whole gearbox, which is due to that the first planetary stage has a large volume and consists of many gears and bearings. Under the nacelle pitch motion, the axial component of the mass of the first planetary stage is significant, which is only carried by the bearing PLC-A, because the downwind bearing PLC-B is a cylindrical roller bearing and has no capacity to carry the axial loads.

Since in the rated wind speed condition, the rotor thrust force reach the peak, which leads to a largest nacelle pitch motion, thus in the Table 11, the largest percentage difference appear in the rated condition. In the Table 12, under the above-rated condition, the small change in different seed conditions is due to that different seeds have a limited effect on the mean level of the pitch motion for a given wind speed condition. As a whole, for the FWT drivetrain design, ignoring the nacelle motions would result in the design deficiency. Particular attentions should be paid on a few bearings in the gearbox, which have the capacity to carry axial force and support heavy structures or mechanical components. When assessing the design or dynamic behaviour of main bearings as well as gears and bearings that only carry radial forces in the gearbox, the nacelle motions could be ignored.

5. Concluding remarks

This study compares the dynamic behaviour of a 10-MW FWT drivetrain predicted by fully coupled and de-coupled dynamic analysis methods. A fully coupled FWT aero-hydro-servo-elastic model is developed in a multi-body system software Simpack by integrating codes of aerodynamics, hydrodynamics and control system, where a high-fidelity drivetrain is also included. The developed fully coupled FWT model is validated from global and local drivetrain perspectives. In the global perspective, a comprehensive code-to-code comparison between the simulation tools Simpack and Fast is carried out. Global performance in terms of decay natural frequencies, power generation, tower top loads, nacelle acceleration and blade pitch angle between these two codes are compared. In the local drivetrain perspective, the first-order

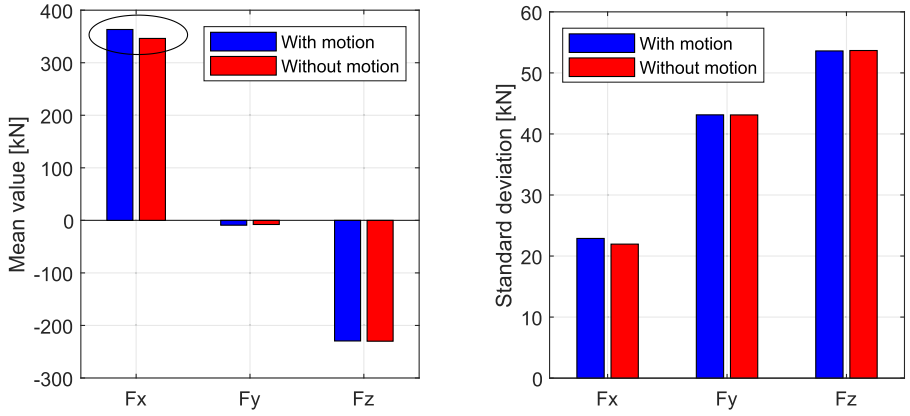

Fig. 17. Comparisons of mean values and standard deviations of the axial and radial forces of the bearing PLC-A between conditions of with and withou nacelle motions in the de-coupled analysis, under the rated load case.

torsional natural frequency of the detailed drivetrain in the fully coupled wind turbine model is compared with that estimated by theoretical method and with that of a single degree-of-freedom drivetrain. The comparisons indicate that the natural characteristics and dynamic behaviour of the 10-MW wind turbine model using both the proposed and reference simulation codes agree well. This demonstrates that results obtained from the proposed fully coupled model are reasonable. Resonance analysis of the drivetrain in the fully coupled model is conducted. One-hour fatigue damge of the drivetrain bearings and gears are compared in the fully coupled and de-coupled models in different environmental conditions. Effect of nacelle motions in the de-coupled analysis is evaluated. The main conclusion are summarized as follows:

- In the 10-MW fully coupled wind turbine model, drivetrain first-order non-torsional natural frequencies are lower than the first-order torsional natural frequency, which makes the drivetrain resonance risk is higher in the non-torsional directions than that in the torsional direction.
- De-coupled analysis method could accurately assess the dynamic behaviour of wind turbine drivetrains. This is because in this study, generally less than 5% percentage difference in 1-h fatigue damage in drivetrain bearings and gears calculated by the fully couple and de-coupled methods is found in different environmental conditions.
- In de-coupled analysis, ignoring nacelle motions, as employed in traditional drivetrain design, will lead to design deficiency of the gearbox in FWTs. Nacelle pitch motion effect should be considered in assessing dynamic behaviour of a few specific gearbox bearings that have capacity to carry the axial force.

This study suggests that the de-coupled method could provide accurate results in the drivetrain fatigue damage if the natural frequencies of the drivetrain are sufficiently separated from that of the "global system". In this 10-MW wind turbine model, the drivetrain resonance does not appear, but the low-order natural frequencies of the drivetrain in non-torsional directions are close to boundary of the rotor excitation frequencies. Particular attentions should be paid on drivetrain resonance check in non-torsional modes, which is essential for the future FWTs with growing size. In the case that drivetrain has resonance in the fully coupled model, the de-coupled method should not be used.

Funding support

Research Council of Norway through Centre for Ships and Ocean Structures (CeSOS) and the Centre for Autonomous Marine Operations and Systems (AMOS), Norwegian University of Science and Technology. China Scholarship Council (CSC) (Grant No. 201706050147)

CRediT authorship contribution statement

Shuaishuai Wang: Conceptualization, Methodology, Software, Formal analysis, Writing – original draft, Writing – review & editing. **Torgeir Moan:** Conceptualization, Methodology, Writing – review & editing, Supervision. **Amir R. Nejad:** Writing – review & editing, Supervision.

Declaration of competing interest

The authors declare that they have no known competing financial interests or personal relationships that could have appeared to influence the work reported in this paper.

Acknowledgment

The first and second authors would like to acknowledge the support from the Research Council of Norway through Centre for Ships and Ocean Structures (CeSOS) and the Centre for Autonomous Marine Operations and Systems (AMOS), Norwegian University of Science and Technology. Moreover, the first author would like to thank the financial support from the China Scholarship Council (CSC) (Grant No. 201706050147).

References

[1] MHI Vestas V174 9.5-MW and V164 10.0-MW wind turbines. http://www.mhivestasoffshore.com/innovations/. (Accessed 6 March 2020).
[2] W. Yu, K. Müller, F. Lemmer, D. Schlipf, H. Bredmose, M. Borg, T. Landbø, H. Andersen, LIFES50+ D4. 2: Public Definition of the Two LIFES50+ 10 MW Floater Concepts, University of Stuttgart.
[3] GE's Haliade-X 12-MW wind turbine. https://www.ge.com/renewableenergy/wind-energy/offshore-wind/haliade-x-offshore-turbine. (Accessed 6 March 2020).
[4] E. Gaertner, J. Rinker, L. Sethuraman, F. Zahle, B. Anderson, G.E. Barter, N.J. Abbas, F. Meng, P. Bortolotti, W. Skrzypinski, et al., IEA Wind TCP Task 37: Definition of the IEA 15-Megawatt Offshore Reference Wind Turbine, Tech. Rep, National Renewable Energy Lab.(NREL), Golden, CO (United States), 2020.
[5] B. Wen, X. Tian, X. Dong, Z. Peng, W. Zhang, K. Wei, A numerical study on the angle of attack to the blade of a horizontal-axis offshore floating wind turbine under static and dynamic yawed conditions, Energy 168 (2019) 1138–1156.
[6] S. Zhou, C. Li, Y. Xiao, P.W. Cheng, Importance of platform mounting orientation of y-shaped semi-submersible floating wind turbines: a case study by using surrogate models, Renew. Energy 156 (2020) 260–278.
[7] J. Azcona, F. Vittori, Mooring system design for the 10 MW triple spar floating wind turbine at a 180 m sea depth location, in: Journal of Physics: Conference Series, vol. 1356, IOP Publishing, 2019, 012003.
[8] V162 5.6-MW wind turbine. https://www.vestas.com/en/products/enventus_platform#!enventus-platform. (Accessed 6 March 2020).
[9] C. Bak, F. Zahle, R. Bitsche, T. Kim, A. Yde, L. C. Henriksen, A. Natarajan, M. H. Hansen, reportDescription of the DTU 10 MW Reference Wind Turbine, DTU Wind Energy Report-I-0092 5.
[10] S. Faulstich, B. Hahn, P.J. Tavner, Wind turbine downtime and its importance for offshore deployment, Wind Energy 14 (3) (2011) 327–337.
[11] Y. Xing, M. Karimirad, T. Moan, Modelling and analysis of floating spar-type wind turbine drivetrain, Wind Energy 17 (4) (2014) 565–587.
[12] A.R. Nejad, E.E. Bachynski, M.I. Kvittem, C. Luan, Z. Gao, T. Moan, Stochastic dynamic load effect and fatigue damage analysis of drivetrains in land-based and TLP, spar and semi-submersible floating wind turbines, Mar. Struct. 42 (2015) 137–153.
[13] Z. Li, B. Wen, K. Wei, W. Yang, Z. Peng, W. Zhang, Flexible dynamic modeling and analysis of drive train for offshore floating wind turbine, Renew. Energy 145 (2020) 1292–1305.
[14] S. Wang, A.R. Nejad, T. Moan, On design, modelling, and analysis of a 10-MW medium-speed drivetrain for offshore wind turbines, Wind Energy 23 (4) (2020) 1099–1117.
[15] S. Wang, A.R. Nejad, E.E. Bachynski, T. Moan, Effects of bedplate flexibility on drivetrain dynamics: case study of a 10 MW spar type floating wind turbine, Renew. Energy 161 (2020) 808–824.
[16] S. Wang, T. Moan, et al., Dynamic behaviour comparison of a 10-mw drivetrain in a bottom-fixed monopile and a spar floating wind turbines, in: The 30th International Ocean and Polar Engineering Conference, International Society of Offshore and Polar Engineers, 2020.
[17] R. Schkoda, A. Bibo, Y. Guo, S. Lambert, R. Wallen, Characterizing the influence of abstraction in full-scale wind turbine nacelle testing, in: ASME 2016 International Design Engineering Technical Conferences and Computers and Information in Engineering Conference, American Society of Mechanical Engineers Digital Collection, 2016.
[18] J. Jonkman, S. Butterfield, W. Musial, G. Scott, Definition of a 5-MW reference wind turbine for offshore system development. Tech. Rep., National Renewable Energy Lab.(NREL), Golden, CO (United States), 2009.
[19] Dr techn, A.S. Olav Olsen. https://www.olavolsen.no. (Accessed 6 January 2020).
[20] LIFES 50+ project. https://lifes50plus.eu. (Accessed 6 January 2020).
[21] L. B. D. GL, Qualification of Innovative Floating Substructures for 10 MW Wind Turbines and Water Depths Greater than 50m.
[22] S. Wang, A.R. Nejad, T. Moan, On initial design and modelling of a 10 MW medium speed drivetrain for offshore wind turbines, in: Journal of Physics: Conference Series, vol. 1356, IOP Publishing, 2019, 012024.
[23] SIMPACK, Multi-body system software. https://www.3ds.com/products-services/simulia/products/simpack/. (Accessed 16 January 2020).
[24] P.J. Moriarty, A.C. Hansen, AeroDyn Theory Manual, Tech. Rep., National Renewable Energy Lab., Golden, CO (US), 2005.
[25] J. M. Jonkman, A. Robertson, G. J. Hayman, HydroDyn User's Guide and Theory Manual, National Renewable Energy Laboratory.

[26] B.J. Jonkman, TurbSim User's Guide: Version 1.50, Tech. Rep, National Renewable Energy Lab.(NREL), Golden, CO (United States), 2009.
[27] A. Pegalajar-Jurado, F. Madsen, M. Borg, H. Bredmose, LIFES50+ D4. 5: State-Of-The-Art Models for the Two LIFES50+ 10 MW Floater Concepts, Tech. Rep., Technical University of Denmark, 2018. Technical Report
[28] C. Lee, J. Newman, WAMIT User Manual, Version 7.0, WAMIT, Inc., Chestnut Hill, MA, 2013.
[29] W. Cummins, The Impulse Response Function and Ship Motions, Tech. Rep., David Taylor Model Basin Washington DC, 1962.
[30] J.M. Jonkman, M.L. Buhl Jr., Fast User's Guide-Updated August 2005, Tech. Rep., National Renewable Energy Lab.(NREL), Golden, CO (United States), 2005.
[31] ISO6336-1, Calculation of Load Capacity of Spur and Helical Gears, Part 6: Basic Principles, Introduction and General Influence Factors, International Organization for Standardization, Geneva, Switzerland, 2006.
[32] D. Matha, U. Fechter, M. Kühn, P. Cheng, Non-linear Multi-Body Mooring System Model for Floating Offshore Wind Turbines, EWEA offshore, 2011.
[33] ISO281, Rolling Bearings-Dynamic Load Ratings and Rating Life, International Organization for Standardization, Geneva, Switzerland, 2007.
[34] A. R. Nejad, Z. Gao, T. Moan, On long-term fatigue damage and reliability analysis of gears under wind loads in offshore wind turbine drivetrains, Int. J. Fatig. 61.
[35] E. Wilkins, Cumulative damage in fatigue, Colloquium on Fatigue/Colloque de Fatigue/Kolloquium über Ermüdungsfestigkeit, Springer, Berlin, Heidelberg, 1956, pp. 321–332.
[36] ISO6336-3, Calculation of Load Capacity of Spur and Helical Gears, Part 3: Calculation of Tooth Bending Strength, International Organization for Standardization, Geneva, Switzerland, 2006.
[37] ISO6336-5, Calculation of Load Capacity of Spur and Helical Gears, Part 5: Strength and Quality of Materials, International Organization for Standardization, Geneva, Switzerland, 2003.
[38] A. Pegalajar-Jurado, H. Bredmose, M. Borg, J.G. Straume, T. Landbø, H.S. Andersen, W. Yu, K. Müller, F. Lemmer, State-of-the-art model for the LIFES50+ OO-Star Wind Floater Semi 10MW floating wind turbine, in: Journal of Physics: Conference Series, vol. 1104, IOP Publishing, 2018, 012024.
[39] IEC61400-1, Wind Turbines, Part 1: Design Requirements, International Electrotechnical Commission, Geneva, Switzerland, 2005.
[40] IEC61400-3, Wind Turbines, Part 3: Design Requirements for Offshore Wind Turbines, International Electrotechnical Commission, Geneva, Switzerland, 2009.
[41] M. Hall, Moordyn User's Guide, Orono, ME: Department of Mechanical Engineering, University of Maine.
[42] S. Wang, T. Moan, Z. Jiang, Effects of uncertainties of environmental conditions on short-term fatigue damage of floating wind turbine drivetrains, Submitted to journal (2020).